

HI Shells and Supershells in the I-GALFA HI 21-cm Line Survey: I. Fast-Expanding HI Shells Associated with Supernova Remnants

G. Park¹, B.-C. Koo^{1,13}, S. J. Gibson², J.-h. Kang^{3,4,5}, D. C. Lane^{3,6}, K. A. Douglas^{3,7}, J. E. G. Peek^{8,9}, E. J. Korpela¹⁰, C. E. Heiles¹¹, J. H. Newton^{2,12}

ABSTRACT

We search for fast-expanding HI shells associated with Galactic supernova remnants (SNRs) in the longitude range $\ell \approx 32^\circ$ to 77° using 21-cm line data from the Inner-Galaxy Arecibo L-band Feed Array (I-GALFA) HI survey. Among the 39 known Galactic SNRs in this region, we find such HI shells in four SNRs: W44, G54.4 – 0.3, W51C, and CTB 80. All four were previously identified in low-resolution surveys, and three of those (excluding G54.4 – 0.3) were previously studied with the Arecibo telescope. A remarkable new result, however, is the detection of HI emission at both very high positive and negative velocities in W44

¹Department of Physics and Astronomy, Seoul National University, 1 Gwanak-ro, Gwanak-gu, Seoul 151-742, Republic of Korea

²Department of Physics and Astronomy, Western Kentucky University, Bowling Green, KY 42101, USA

³Arecibo Observatory, HC 3 Box 53995, Arecibo, PR 00612, USA

⁴Yonsei University Observatory, Yonsei University, 50 Yonsei-ro, Seodaemun-gu, Seoul 120-749, Republic of Korea

⁵Korea Astronomy and Space Science Institute, 776 Daedeokdae-ro, Yuseong-gu, Daejeon 305-348, Republic of Korea

⁶Department of Electrical and Computer Engineering, San Diego State University, San Diego, CA 92182, USA

⁷University of Calgary/Dominion Radio Astrophysical Observatory, P.O. Box 248, Penticton, BC V2A 6J9, Canada

⁸Department of Astronomy, Columbia University, New York, NY 10027, USA

⁹Hubble Fellow

¹⁰Space Sciences Laboratory, University of California, Berkeley, CA 94720, USA

¹¹Radio Astronomy Lab, UC Berkeley, 601 Campbell Hall, Berkeley, CA 94720, USA

¹²Department of Physics and Astronomy, McMaster University, Hamilton, Ontario L8S 4M1, Canada

¹³Corresponding author; koo@astro.snu.ac.kr

from the receding and approaching parts of the HI expanding shell, respectively. *This is the first detection of both sides of an expanding shell associated with an SNR in HI 21-cm emission.* The high-resolution I-GALFA survey data also reveal a prominent expanding HI shell with high circular symmetry associated with G54.4–0.3. We explore the physical characteristics of four SNRs and discuss what differentiates them from other SNRs in the survey area. We conclude that these four SNRs are likely the remnants of core-collapse supernovae interacting with a relatively dense ($\gtrsim 1 \text{ cm}^{-3}$) ambient medium, and we discuss the visibility of SNRs in the HI 21-cm line.

Subject headings: ISM: supernova remnants — Galaxy: disk — radio lines: ISM

1. Introduction

The interstellar medium (ISM) is pervaded by small and large expanding neutral atomic shells (e.g., Heiles 1979, 1984; McClure-Griffiths et al. 2002; Ehlerová & Palouš 2005; McClure-Griffiths 2012). These HI shells are the interstellar material swept up by supersonic shock waves produced by mechanical energy sources, including HII regions, stellar winds, supernova (SN) explosions, and infalling high-velocity clouds. The dominant and most violent sources are supernovae (SNe), which dump huge amounts of kinetic energy into the Galactic ISM every 20–70 yrs. But it is not clear how this kinetic energy is conveyed to the diffuse ISM, because this depends on the types and the physical environments of SNe. Most supernovae are core-collapse SNe (CCSNe) that have massive ($\geq 8 M_{\odot}$) progenitors, and most CCSNe are produced in clusters (e.g., Higdon & Lingenfelter 2005). Most SN explosions, therefore, are correlated in both space and time, with such groupings frequently producing supershells and superbubbles with radii of more than a few hundred parsecs. Only Type Ia SNe and a small fraction of CCSNe are likely to occur in isolation. Single CCSNe probably explode inside a wind bubble created by their progenitor stars during the main-sequence phase. For stars of spectral type later than B0, this bubble size is small ($\lesssim 1 \text{ pc}$), and the SNRs can interact with dense molecular clouds in their early evolution (Chevalier 1999). Type Ia’s, on the other hand, probably explode in either warm diffuse environments of density $n \sim 0.1 \text{ cm}^{-3}$ or in hot, rarefied gas with $n \sim 10^3 \text{ cm}^{-3}$. The amount and characteristics of the kinetic energy imparted to the ISM by SNe, therefore, should be diverse, and their role in shaping the kinematics of the atomic phase of the ISM is not clear. Consequently, HI observations of shells and supershells are useful not only to understand the nature and origin of individual structures but also, with reasonably large statistical samples, to explore the overall effects of SNe on the ISM.

There have been a number of systematic searches for HI shells associated with individual Galactic SNRs. Koo & Heiles (1991, hereafter KH91) carried out a survey of Galactic SNRs in HI 21-cm line using the Hat-Creek 25 m telescope (FWHM= 36'). They observed 103 northern Galactic SNRs and detected high-velocity (HV) gas toward 15 SNRs including three SNRs known prior to the survey. Koo et al. (2004) searched for similar HI features toward 97 southern SNRs using the Parkes data from the Southern Galactic Plane Survey (FWHM= 16'; McClure-Griffiths 2001) and identified another 10 SNRs. Since the SNRs are usually less than 1° in diameter, high-resolution observations are essential to confirm the association of HV HI features with the radio continuum SNR. Such confirmations have been made in several cases, e.g., CTB 80 (Koo et al. 1990), W44 (Koo & Heiles 1995), W51C (Koo & Moon 1997a), and IC 443 (Giovanelli & Haynes 1979; Braun & Strom 1986; Lee et al. 2008). There have also been studies of almost stationary HI shells or HI bubbles associated with SNRs, but it is generally difficult to derive the parameters of such low-velocity HI shells due to HI background confusion (e.g., Kothes et al. 2005; Cazzolato & Pineault 2005; see also references in Koo et al. 2004).

Recently, the 7-beam Arecibo L-band Feed Array (ALFA) receiver on the Arecibo 305m telescope has enabled Galactic HI surveys of unprecedented breadth and sensitivity with a fully-sampled 4' beam (Peek et al. 2010, 2011). The Inner Galaxy ALFA (I-GALFA) survey (Koo et al. 2010; Gibson et al. 2012) covers the portion of the first Galactic quadrant visible to Arecibo, an area of more than 1650 square degrees at longitudes of 32° to 77° in the Galactic plane and extending to 10° or more off the plane. I-GALFA uses 0.184 km s⁻¹ velocity channels over an LSR velocity range of ~ -700 to $+700$ km s⁻¹. Its brightness temperature RMS noise is 0.2 K in single empty channels. This combination of high sensitivity, high spatial and spectral resolution, and large area and velocity coverage are well suited for a systematic study of HI shells and supershells in the diffuse interstellar medium. In this first paper, we search for fast-expanding HI shells associated with *known* SNRs and consider the implications of our results on their nature. A forthcoming paper will discuss known HI shells and supershells as well as newly identified shells in the I-GALFA survey data. It is worth noting that the VLA Galactic Plane Survey (VGPS; Stil et al. 2006) and Canadian Galactic Plane Survey (CGPS; Taylor et al. 2003) cover most of the SNRs in the first quadrant in HI at higher spatial resolution ($\sim 1'-2'$). Their velocity coverage and sensitivity ($\pm 100-150$ km s⁻¹ and 1-3 K per 0.8 km s⁻¹ channel) are not ideal to study faint, fast-expanding HI shells, but they can be useful to study shell fine structure at relatively low velocities.

In Section 2, we explain how we identify fast-expanding HI shells associated with SNRs and present the resulting list. In Section 3, we summarize the results on four SNRs that have associated fast-expanding HI shells. The two SNRs with new results, W44 and G54.4 – 0.3,

are discussed in some detail. In Section 4, we explore the physical characteristics of the four SNRs and compare their properties to the other 35 SNRs in the survey area. Section 5 summarizes the paper.

2. Identification of SNR HI shells

There are 275 Galactic SNRs in Green’s catalog (Green 2009a,b). Among them, 39 SNRs are included in the I-GALFA area (Table 1). The SNR name, size, and type parameters in Table 1 are from Green (2009a). (See the table note for more parameter details.) Note that the 21-cm spectra of sources with high continuum brightness are noisy, so faint high-velocity emission could not be seen in those objects. In Table 1, the ranks determined by KH91 are also listed. KH91 observed each SNR with the Hat Creek 85-foot telescope (FWHM=36′) at 9 points in a cross pattern centered on its catalog position and searched for SNRs with broad ($\simeq 10 \text{ km s}^{-1}$) excess emission over the background. They divided SNRs into four ranks: 0, 1, 2, and 3, where rank 3 has the highest probability for an associated fast-expanding HI shell. In rank 1, the central excess emission is brighter than the four outermost positions; in rank 2, the central excess emission is brighter than all outer positions; in rank 3, there is also excess emission at the highest positive or negative velocities; and in rank 0, none of these criteria are met. Among 39 sources in Table 1, 26 were studied by KH91, who classified 9 of these as rank 3 SNRs. KH91 mapped the excess HV emission in these 9 SNRs and concluded that the HI emission is not physically associated in 4 cases (marked as ‘(3)’ in Table 1). Four SNRs are in rank 2. The other 13 (ranks 1 and 0) did not show any significant excess HI emission.

In order to identify fast-expanding shells associated with SNRs, we examined whether enhanced emission is present at the SNR position at high positive/negative velocities in several ways. We first inspected average, background-subtracted HI spectra toward individual SNRs as KH91 did. The average spectrum was obtained from a circular area with 1.1 times the SNR radius, while the background spectrum was obtained from an annular ring of 3′ thickness surrounding the SNR. The radial interval between the SNR circle and the background ring was either 9′ or 0.5 times the SNR radius, whichever was smaller. If another bright radio continuum source was located near the SNR, we left an appropriate space between the SNR circle and the background ring. We confirmed that all SNRs classified as rank 3 by KH91 show excess emission at high positive/negative velocities in their background-subtracted spectra, but we could not find additional SNRs with such features.

The above approach could have missed associated HI emission limited to small areas. We therefore inspected individual channel maps as well as (ℓ, v) and (b, v) maps to search

for HV HI emission features spatially correlated with the SNRs in radio continuum maps. These are mostly from the VGPS or CGPS 21-cm continuum data with $\sim 1'$ resolution. For SNRs outside these two survey areas, we used either the lower-resolution ($\sim 4'3$) Effelsberg 11-cm continuum data (Reich et al. 1990) or referred to previous works. Surprisingly, this detailed inspection yielded no additional detections. Instead, we confirmed the conclusion of KH91 that the HV emission in four rank 3 SNRs extended beyond the spatial extent of SNRs, so that it was probably not associated with the SNRs (marked as ‘(3)’ in Table 1). In one of them (G40.5 – 0.5), we found that the HV HI emission is part of a much larger and prominent expanding shell. This result will be discussed in a forthcoming paper.

We are therefore left with the five rank 3 SNRs of KH91, but we suspect the HV HI emission in W50 (G39.7 – 2.0) is probably not associated with the SNR. W50 is a large, elongated shell-like SNR with SS 433 at the center, and KH91 reported the presence of very weak, extended HI emission at high positive velocities along the northern edge of the SNR where the continuum emission is enhanced (cf. Lockman et al. 2007). The high-resolution I-GALFA data confirm the presence of weak, filamentary HI emission along the SNR edge that appears connected to other HI structures well outside the SNR. We therefore regard the spatial correlation between the HI emission and the SNR as a coincidence. Our results are summarized in the last column of Table 1, where we comment only on the HV emission features. We do see some low-velocity HI features that may be associated with SNRs, but many of these are confusing, and the scope of the present paper is limited to *fast-expanding* HI shells in SNRs.

3. Supernova Remnants with Fast-Expanding HI Shells

We have identified four SNRs that have associated HV HI gas: G34.7 – 0.4 (W44), G49.2 – 0.7 (W51C), G54.4 – 0.3 (HC40), and G69.0 + 2.7 (CTB 80). All four were ranked 3 by KH91, and follow-up high resolution observations have been made for SNRs W44, W51C, and CTB 80 (Koo & Heiles 1995; Koo & Moon 1997a; Koo et al. 1993). Figure 1 shows their average HI line profiles while Figure 2 shows (ℓ, v) maps across the centers of these four SNRs. (See Figure 3 for the areas used to derive these profiles.) The average profiles show some fluctuations in baseline, but they are removed in background-subtracted profiles. Figures 1 and 2 show that these four SNRs have excess HI emission at highest positive velocities. In W44, a faint, but clear, excess emission at highest negative velocities is also visible. Integrated (ℓ, b) maps in Figure 3 show the spatial distribution of HV HI emissions. The overlaid radio contours of SNRs clearly show that the HV HI gas is confined inside the SNR boundaries of W44 and G54.4 – 0.3. We discuss W44 and G54.4 – 0.3 in some detail

below, where new results are obtained. We also briefly comment on the other two SNRs, W51C and CTB 80, where the I-GALFA results agree with previous findings.

3.1. W44 (G34.7 – 0.4)

3.1.1. Previous studies

W44 is a middle-aged SNR ($\sim 2 \times 10^4$ yr) of mixed morphology, being shell-type in radio continuum but centre-filled in X-rays (Rho & Petre 1998). The radio continuum shell is somewhat elongated ($35' \times 27'$), and the southeastern¹ portion of the SNR shows enhanced radio emission (Figure 3; see also Castelletti et al. 2007). The pulsar PSR 1853+01 with a spin-down age of $\sim 2 \times 10^4$ yr lies $9'$ southwest of the center of W44, embedded in an X-ray emitting pulsar wind nebula (Petre et al. 2002; Wolszczan et al. 1991). HI gas at very high positive velocities ($\gtrsim +130$ km s⁻¹) accelerated by the SNR shock has been detected inside the remnant and studied using the Arecibo telescope (Koo & Heiles 1995). Ample evidence indicates the SNR is interacting with a molecular cloud in the southeast at $v_{\text{LSR}} = +46.6$ km s⁻¹ (Seta et al. 1998; Reach et al. 2005, and references therein). An extensive, organized system of thin and knotty H₂ filaments filling the SNR may indicate that the SN exploded inside a molecular cloud (Reach et al. 2005; Froebrich et al. 2011). Gamma-ray emission from the SNR has been detected by *Fermi*/LAT and *AGILE*/GRID at 50 MeV–10 GeV (Abdo et al. 2010; Giuliani et al. 2011). The emission is confined to an incomplete ring structure that matches well with the SNR but with a slight offset. The gamma-ray spectrum is well modeled with emission from cosmic-ray protons interacting with the nuclei in the ambient medium. Distance estimates to the SNR range from 2.6 to 3.2 kpc.

3.1.2. New Results

The I-GALFA images reveal several new HI features not seen in previous studies. First, we detect fast-moving HI gas associated with the SNR at both the highest positive and highest negative velocities. The negative-velocity emission is relatively faint, but clearly real (see below). The HI gas at positive and negative velocities must be from the receding and approaching hemispheres of the SNR, respectively. *This is the first detection of both sides of an expanding SNR shell in the HI 21-cm emission line.* We will discuss the visibility of fast-expanding HI shells in § 4.2.

¹Directions in this paper are all in reference to Galactic coordinates, not J2000 Equatorial coordinates.

Figure 4 shows channel maps at both negative and positive velocities where we see HI emission confined inside the SNR boundary. At the highest negative velocities (-120 to -100 km s $^{-1}$), a knotty, elongated emission feature is seen along the southeastern boundary of the SNR (blue arrow in first two panels). It is worth noting that this is where the SNR is currently interacting with the molecular cloud (see references in the previous paragraph). At velocities less negative than this, the emission in the central area has a ring-like shape. At positive velocities, the HI emission is more prominent. At the highest positive velocities, the HI gas is confined to the central area of the remnant with the ring-like morphology noted by Koo & Heiles (1995). And at $v_{\text{LSR}} = +130$ km s $^{-1}$, the HI gas forms a ring structure along the inner boundary of the SNR. This indicates that the HI gas is part of an expanding shell, and that the size of the HI shell is comparable to the radio continuum shell. This is in contrast to Koo & Heiles (1995), who concluded that the HI shell was smaller than the continuum shell from the extrapolation of the HI gas distribution at the highest velocities. Figure 4 indeed shows that the HI ring structure rather abruptly shifts from the central region to the SNR boundary as the velocity changes from $+137$ to $+130$ km s $^{-1}$. We speculate that the total extent of the expanding HI shell is probably comparable to the radio continuum shell, but the shell is not complete.

Figure 5 shows the average HI profile of W44. If the HI shell is symmetric, we can in principle derive an accurate systemic velocity by measuring the velocity at which the line profile becomes symmetric. For example, if we naively fit a Gaussian to the line profile, we obtain a central velocity of $+59$ km s $^{-1}$, which is considerably higher than the systemic velocity ($+47$ km s $^{-1}$) of the associated molecular cloud. We attribute the discrepancy to the asymmetric mass distribution of the HI shell. The implied asymmetry also makes it difficult to derive an accurate mass. But the uncertainty in the mass estimation is mainly due to the unobservable mass at low velocities, and, by fixing the central velocity, we can derive a reasonably accurate mass. The average line profile becomes flattened at velocities below $+160$ km s $^{-1}$, i.e., it does not rise steeply as one might expect when the high-velocity part (≥ 160 km s $^{-1}$) is the tail of a Gaussian profile, which is consistent with Koo & Heiles (1995). If the HI shell is uniform and expanding at a constant speed v_{exp} , then the average HI 21-cm line profile would appear as a square profile that extends from $-v_{\text{exp}}$ to $+v_{\text{exp}}$ centered at the systemic velocity v_0 (e.g., see Koo & Heiles 1991), i.e.,

$$T_{b,\text{square}}(v) = \begin{cases} T_{b,\text{max}} & \text{for } v_0 - v_{\text{exp}} \leq v \leq v_0 + v_{\text{exp}} \\ 0, & \text{otherwise} \end{cases} \quad (1)$$

where $T_{b,\text{max}}$ is the maximum brightness temperature, which is proportional to the total mass in the shell (see below). But the shell probably does not coast at a constant speed, given non-uniformity/inhomogeneity of the ambient medium, turbulent motions produced

by hydrodynamic instabilities, etc. We assume that the observed profile is composed of a flat profile convolved by a Gaussian profile, i.e.,

$$T_b(v) = \int_{-\infty}^{+\infty} T_{b,\text{square}}(u) \exp\left[\frac{-(v-u)^2}{2\sigma_v^2}\right] du \quad (2)$$

where σ_v is the dispersion of random velocities related to the velocity at Full-Width at Half Maximum (FWHM) Δv_{FWHM} by $\sigma_v = \Delta v_{\text{FWHM}}/2\sqrt{2 \ln 2}$.

The fast-moving gas is clumpy and has broad lines. In the SNR W51C, for example, Koo & Moon (1997a) resolved individual clumps using the VLA and found that their line profiles have FWHM of $\sim 40 \text{ km s}^{-1}$. In the I-GALFA survey, we could not completely resolve out clumps from the background emission in velocity space. But we see many clumps that appear as prominent protrusions. Figure 6 shows some examples of HV bumps in the tails of strong background emission. We fit the HV parts of these spectra with several Gaussian components. Our purpose is only to obtain the widths of the HV bumps, so the fit parameters of the low-velocity components are unimportant. We obtain suitable results using four components for CTB 80 and three for the others (Figure 6), and we find $\Delta v_{\text{FWHM}} \approx 50 \text{ km s}^{-1}$ for the HV components in all four SNRs. We adopt $\Delta v_{\text{FWHM}} = 50 \text{ km s}^{-1}$ as the characteristic value for the fit. The large velocity dispersion within the shell implies that the shell is dispersing, but its thickness will remain small compared to the radius of the shell until the very late stage of SNR evolution.

With the systemic velocity fixed at $v_0 \equiv +47 \text{ km s}^{-1}$, we vary $T_{b,\text{max}}$ and v_{exp} . The fit was done using the IDL routine MPFIT (Markwardt 2009). The best fit profile is shown in Figure 5. Its parameters are $v_{\text{exp}} = 135 \pm 2 \text{ km s}^{-1}$ and $T_{b,\text{max}} = 0.168 \pm 0.005 \text{ K}$. The HI mass is derived from the average column density obtained from the fit, i.e., $\bar{N}_{\text{H}} = 1.822 \times 10^{18} T_{b,\text{max}} \times 2v_{\text{exp}} \text{ cm}^{-2}$ considering both approaching and receding sides of the shell, by multiplying the area of W44. (Since the peak brightness temperature is only $\sim 0.2 \text{ K}$, we may assume that the HI emission is optically thin.) The derived HI mass is $393 \pm 13 M_{\odot}$, which implies a kinetic energy of $9.9 \pm 0.4 \times 10^{49} \text{ erg}$. These numbers agree with those of Koo & Heiles (1995) within 10–20%. The resulting dynamical age of the shell is $t \simeq 0.3R_s/v_s \simeq 2.7 \times 10^4 \text{ yr}$ (Cioffi et al. 1988), where we used a geometrical mean radius (12.5 pc at 2.8 kpc; See Tables 2 and 3 for the adopted distances to the SNRs) as the radius of the SNR, R_s . This dynamical age is somewhat larger than the characteristic spin-down age of the pulsar. Assuming that this mass was initially inside the volume of the SNR, i.e., inside a sphere of geometrical radius of 12.5 pc, the mean density of hydrogen nuclei in the ambient medium would be $1.9 \pm 0.1 \text{ cm}^{-3}$. The initial explosion energy, E_{SN} , can be estimated from

$$E_{\text{SN}} = 6.8 \times 10^{43} n_0^{1.16} R_s^{3.16} v_{\text{exp}}^{1.35} \text{ erg}, \quad (3)$$

where n_0 is the ambient density of hydrogen nuclei in cm^{-3} , R_s is in pc, and v_{exp} is in km s^{-1} (Cioffi et al. 1988). We assume solar metallicity. Substituting the derived values, i.e., $n_0 = 1.9 \text{ cm}^{-3}$, $R_s = 12.5 \text{ pc}$, and $v_{\text{exp}} = +135 \text{ km s}^{-1}$, we have $E_{\text{SN}} = 3.2 \pm 0.1 \times 10^{50} \text{ erg}$. This is the energy required to heat and accelerate more or less uniformly distributed atomic gas. Since there is also fast-expanding ($\sim +30 \text{ km s}^{-1}$), dense molecular gas accelerated by SN blast wave (Reach et al. 2005; Froebrich et al. 2011), some fraction of the total SN energy should have been used up for heating and accelerating the molecular gas. It would be interesting to derive the kinetic energy of shocked H_2 filaments and compare it to that of the HI shell.

3.2. G54.4 – 0.3 (HC 40)

3.2.1. Previous studies

G54.4 – 0.3 is a shell-type SNR of circular shape with a diameter of $40'$. The shell is not complete, and its radio continuum brightness is not uniform (see the contour map in Figure 3; Junkes et al. 1992a). In the southeastern part of the remnant, the circular portion of the shell is missing, and instead faint continuum structures are visible connected to the tips of the bright ends. This probably indicates that the SNR blew out in this direction, presumably on encountering a rarefied medium there, and the shell was disrupted in the process. Junkes et al. (1992a) carried out CO observations and suggested an association with a molecular cloud at $v_{\text{LSR}} = +36$ to $+44 \text{ km s}^{-1}$. They proposed a distance of 3 kpc using the rotation curve of Burton (1988). Case & Bhattacharya (1998) adjusted this distance by adopting a revised rotation curve with $R_{\odot} = 8.5 \text{ kpc}$ and $\Theta_{\odot} = 220 \text{ km s}^{-1}$ and obtained 3.3 kpc. If we use the rotation curves of Brand & Blitz (1993) or Levine et al. (2008), the near-side kinematic distance corresponding to the systemic velocity of $+40 \text{ km s}^{-1}$ in this direction is 3.9 and 3.1 kpc, respectively. We adopt the 3.3 kpc distance of Case & Bhattacharya (1998) in this paper. There are several HII regions in this area at about the same distance, including the compact HII region just outside the northwestern boundary of the remnant (Junkes et al. 1992b). Junkes (1996) observed the remnant with *ROSAT* and derived an absorbing hydrogen column density of $1 \times 10^{22} \text{ cm}^{-2}$ and a plasma temperature of $2 \times 10^7 \text{ K}$. Boumis et al. (2005) detected optical emission lines in the northwestern edge of the shell and derived an absorbing hydrogen-nuclei column density of $2.9\text{--}4.0 \times 10^{22} \text{ cm}^{-2}$. KH91 detected fast-moving HI gas at velocities $+91$ — $+108 \text{ km s}^{-1}$.

3.2.2. *New Results*

This SNR has some of the most prominent HI shell structure in our sample. Figure 7 shows HI channel images of G54.4 – 0.3 at $v_{\text{LSR}} = +53$ to $+108$ km s⁻¹. At the highest positive velocities, e.g., $v_{\text{LSR}} = +100$ km s⁻¹, the HI gas is confined to the central area of the remnant, whereas at lower velocities, we see a well-defined ring structure as well as some emission filling the central area. This velocity structure indicates that the HV gas is the receding portion of an expanding shell. The shell has non-uniform brightness. A prominent feature is the bar-like structure extending from the center to the southwestern at $v_{\text{LSR}} = +78$ to $+93$ km s⁻¹ (blue arrow in a panel at $+89$ km s⁻¹). Its northeastern tip appears as a bright spot at $(54.^\circ35, -0.^\circ30)$ at $v_{\text{LSR}} = +82$ – $+89$ km s⁻¹. At low velocities, e.g., at $v_{\text{LSR}} = +64$ – $+78$ km s⁻¹, we see some correspondence between HI and radio continuum structures. First, the same southeastern portion of the HI shell is also weak and missing as in the continuum shell. Second, there is faint but enhanced HI emission coincident with the continuum shell at ≥ 70 km s⁻¹. Third, along the southwestern SNR shell, there is a larger filamentary HI structure just outside it at $v_{\text{LSR}} = +64$ to $+78$ km s⁻¹. This external HI feature has the same curvature as the SNR shell, so it might be associated with the SNR too. Perhaps this is the boundary of the stellar wind bubble produced by the progenitor star, although it is not obvious how we can see the SNR shell inside a wind bubble.

We derive the mass of the G54.4 – 0.3 HI shell in a similar fashion to W44, but using only positive velocities. We adopt $\Delta v_{\text{FWHM}} = 50$ km s⁻¹ and assume a systemic velocity of $+40$ km s⁻¹. The best-fit profile, shown in Figure 8, uses $v_{\text{exp}} = 59 \pm 6$ km s⁻¹ and an HI mass of $580 \pm 150 M_\odot$ at 3.3 kpc. The corresponding kinetic energy is $2.8 \pm 0.9 \times 10^{49}$ erg. The resulting dynamical age of the shell is $t \simeq 0.3R_s/v_s \simeq 9.5 \times 10^4$ yr, where we used $R_s = 19.2$ pc ($20'$). Again assuming that this mass was initially inside the volume of the SNR, the mean density of hydrogen nuclei in the ambient medium would be 0.79 ± 0.20 cm⁻³. With the above parameters, we obtain $E_{\text{SN}} = 1.5 \pm 0.5 \times 10^{50}$ erg. This is considerably smaller than the canonical value of 1×10^{51} erg but not unreasonable.

3.2.3. *Others*

G49 – 0.7 (W51C) is a middle-aged, shell-type SNR interacting with a molecular cloud. Koo & Moon (1997a,b) obtained high-resolution HI and CO observations and developed a model in which the fast-moving HI gas is produced by the SNR shock propagating into a molecular cloud. The SNR is one of the most luminous γ -ray sources in the Galaxy (Abdo et al. 2009). The I-GALFA results for the HV HI gas in Figures 1–3 agree with previous results.

G69.0+2.7 (CTB 80) is one of the first infrared SNRs detected by *IRAS* (Fesen et al. 1988). It appears as a large ($\sim 1^\circ$), spherical shell-type SNR in IR while, in radio continuum, only the northern portion of the shell is bright due to the interaction with the pulsar. Koo et al. (1990, 1993) carried out HI studies using the Arecibo telescope and the VLA and confirmed the large size of the SNR shell and its old age ($\sim 1 \times 10^5$ yr). Again, the I-GALFA HV HI results in Figures 1–3 agree with previous results.

4. Discussion

4.1. Properties of HI SNRs

We have detected 4 SNRs with fast expanding HI shells in the I-GALFA survey area. Table 2 summarizes their parameters: distance d , radius R_s , systemic velocity v_0 , expansion speed v_{exp} , dynamical age, HI mass, kinetic energy, ambient density n_0 , and initial explosion energy E_{SN} . The table also lists whether the remnant has an associated pulsar and whether it is interacting with a molecular cloud. The parameters of W44 and G54.4 – 0.3 are those derived in this work, whereas those of W51C and CTB 80 are from previous studies.

There are several points to make. First, all 4 SNRs are middle-aged ($1.8\text{--}9.5 \times 10^4$ yr). Second, the ambient densities are $\gtrsim 1 \text{ cm}^{-3}$, considerably larger than the densities of either the warm or hot diffuse ISM filling most of the interstellar volume. In particular, three SNRs are interacting with molecular clouds. Third, two SNRs are the remnants of core-collapse SNe with associated pulsar wind nebulae (PWNe). The other two remnants, G54.4 – 0.3 and W51C, do not have associated PWNe, but their interactions with molecular clouds suggests they also likely have massive progenitors. In summary, the SNRs with HI shells (hereafter HI SNRs) that are detected are middle-aged SNRs of probable CCSN origin interacting with a relatively dense medium.

The dynamical evolution of middle-aged SNRs in a uniform medium was studied in detail by Cioffi et al. (1988), who derived analytic expressions for radius R_s and expansion velocity v_s that describe the results of their one-dimensional numerical simulations. Koo & Kang (2004) proposed somewhat simpler but still accurate forms of the equations of Cioffi et al. (1988).² We find it useful to introduce a parameter $\delta \equiv n_0 E_{51}^{-0.861}$ where n_0 is the density of hydrogen nuclei in the ambient medium divided by 1 cm^{-3} , and E_{51} is the SN energy released to the ISM in units of 10^{51} erg. Note that δ is dimensionless. The advantage of

² There was a typo in equation (8) of Koo & Kang (2004): the index “-1/14” should be read as “1/14”.

introducing δ is that the radius and velocity of middle-aged SNRs are now related by

$$R_s = 25.7\delta^{-0.367}v_{s,2}^{-3/7} \text{ pc}, \quad (4)$$

where $v_{s,2} \equiv (v_s/100 \text{ km s}^{-1})$. This equation is obtained by combining equations (5)–(8) of Koo & Kang (2004). (Note that this is just another expression of equation (3) except that their numerical coefficients differ by 2%.) In the (R_s, v_s) plane, HI SNRs evolve along a line satisfying the above equation. In terms of δ , the expansion velocity of HI SNRs is given by (Eq. 6 of Koo & Kang 2004)

$$v_s = 179 \delta^{1/7} E_{51}^{0.194} \left(\frac{11}{10} \frac{t}{t_{\text{sf}}} - \frac{1}{10} \right)^{-7/10} \text{ km s}^{-1}, \quad (5)$$

where the “shell formation time” t_{sf} representing the onset of the formation of HI shell is defined by (Cioffi et al. 1988)

$$t_{\text{sf}} \equiv 3.61 \times 10^4 n_0^{-4/7} E_{51}^{3/14} \text{ yr} . \quad (6)$$

As pointed out by Koo & Kang (2004), the maximum disagreement between the equations (4)–(5) and the original equations (3.22)–(3.23) of Cioffi et al. is less than 0.1% during $t \sim (1 - 13)t_{\text{sf}}$. The radius and velocity are now functions of δ , E_{51} , and t/t_{sf} instead of n_0 , E_{51} , and t . And since the dependence of v_s on E_{51} is weak, a single grid can be drawn in the (R_s, v_s) plane to describe the evolution of HI SNRs in different physical environments.

Figure 9 shows how the radius and velocity of HI SNRs evolve in time (t/t_{sf}) for a given δ . The SNR develops a fast-expanding HI shell at $t/t_{\text{sf}} = 1$, which expands and slows down along a line of constant δ as it evolves. For example, suppose an SNR has $E_{51} = 1$ in a uniform medium with $n_0 = 1$, so that $\delta = 1$. Then the SNR has an HI shell of $(R_s, v_s) = (20 \text{ pc}, +179 \text{ km s}^{-1})$ at $t/t_{\text{sf}} = 1$ and $(R_s, v_s) = (40 \text{ pc}, +34 \text{ km s}^{-1})$ at $t/t_{\text{sf}} = 10$, where $t_{\text{sf}} = 3.61 \times 10^4 \text{ yr}$. The HI SNRs identified in the I-GALFA survey have radii of 6–19 pc and expansion velocities $+59 - +135 \text{ km s}^{-1}$, or $\delta = 5-50$ and $t/t_{\text{sf}} = 2-9$. The expansion velocities of the detected HI shells are all greater than $+50 \text{ km s}^{-1}$, which is necessary to be clearly discernible from the Galactic background emission (see next section). It is also worth noting that no large HI SNRs expected in the diffuse ISM have been detected, i.e., there are no HI SNRs where $\delta < 1$ in Figure 9. This may be either because such SNRs are rare or because such SNRs are faint in radio continuum and “missed” in the current catalog of SNRs. We will discuss this further in next section.

4.2. Visibility and Statistics of HI SNRs

The visibility or detectability of SNRs in the HI 21-cm line was investigated by Koo & Kang (2004). An important constraint on the visibility of HI SNRs is that they should be in the

“right” positions in the Galaxy where the line-of-sight velocities of expanding HI shells can easily exceed the maximum or minimum LSR velocities of the Galactic background HI emission, e.g., along the loci of tangential points in the inner Galaxy. For example, W51C is in a high-visibility location, because its systemic velocity ($+62 \text{ km s}^{-1}$) is close to the maximum velocity ($\sim +90 \text{ km s}^{-1}$; see Figure 2) of the background emission in this direction ($\ell = 49.^\circ 2$). In contrast, W44 is in a low-visibility location: its systemic velocity ($+47 \text{ km s}^{-1}$) is much less than the maximum velocity ($+130 \text{ km s}^{-1}$) in this direction ($\ell = 34.^\circ 7$). Apparently, W44 is relatively young and has the largest expansion velocity, so that both its approaching and receding parts can be seen.

The locations of the SNRs in the I-GALFA area are marked in Figure 10 (left), with filled circles for the 4 HI SNRs. Table 3 lists our adopted distances, where the fifth column gives the distances that are considered to be reliable. Twenty-eight SNRs have reliable distances, half of which are from the compilation by Green (2009a). The other half are from our own literature search, with references listed in the last column. The sixth column gives distances estimated using the surface brightness – diameter ($\Sigma - D$) relation (e.g., Case & Bhattacharya 1998; Arbutina et al. 2004; Guseinov et al. 2003). For this work, we adopt the Case & Bhattacharya (1998) version. The $\Sigma - D$ relation has considerable dispersion, and its applicability has been criticized (e.g., Green 2004). But without any other estimates, it still provides a useful reference. We use reliable distances wherever possible and $\Sigma - D$ distances for other SNRs.

The background grey-scale map in Figure 10 (left) shows the minimum shell expansion velocity for detection, $v_{\text{det,min}}$. The Galactic disk is assumed to be axi-symmetric with radius 15 kpc and a flat rotation curve with $R_\odot = 8.5 \text{ kpc}$ and $\Theta_\odot = 220 \text{ km s}^{-1}$. An expanding HI shell is considered to be visible if the LSR velocity of its receding endcap, which is the sum of the systemic LSR velocity and the expansion velocity, is greater than the maximum LSR velocities allowed by circular rotation in that direction by more than 50 km s^{-1} or vice versa. This appears to be conservative considering that the turbulent velocity dispersion of the warm neutral medium is 27 km s^{-1} (Heiles & Troland 2003) and that the non-circular velocities due to spiral shocks are typically 20 km s^{-1} (e.g., Roberts 1969). But note that the HI emission from fast-expanding SNR shells appears as very weak broad wings superposed on the Gaussian tails of background emission; in Figure 6, for example, the maximum LSR velocities in the directions of the four SNRs according to the flat rotation curve are, in the order of increasing Galactic longitude, $+94$, $+54$, $+42$, and $+15 \text{ km s}^{-1}$, respectively. HI shells along the tangent points in the inner Galaxy have small $v_{\text{det,min}}$ ($\sim 50 \text{ km s}^{-1}$) because their positive-velocity wings can be easily detected. The HI shells near the outer boundary of the disk in the survey area also have small $v_{\text{det,min}}$, but, in this case, it is because their negative velocity wings can be easily detected. In order to help the understanding,

Figure 10 (right) shows the variation of $v_{\text{det,min}}$ for SNRs in the direction at $\ell = 32^\circ$. In the top and middle frames, the dotted line shows how the systemic LSR velocity (v_{sys}) varies with distance from the Sun due to Galactic rotation. Note that the maximum and minimum systemic LSR velocities in this direction are 103 and -56 km s^{-1} , respectively. This gives an approximate velocity range of the background HI emission. Therefore, for the receding portion of an expanding SNR shell to be detectable, its expansion velocity should be larger than $(103 + 50) \text{ km s}^{-1} - v_{\text{sys}}$, where v_{sys} is the systemic velocity of the shell (red line in the top frame). On the other hand, for the approaching portion to be detectable, which will appear as a negative-velocity wing, the expansion velocity should be larger than $|(-103 - 50) \text{ km s}^{-1} - v_{\text{sys}}|$ (blue line in the middle frame). For just one part of the shell detectable, the required expansion velocity will be the smaller of the two (thick line in the bottom frame). Figure 10 shows that three SNRs (W51C, G54.4 – 0.3, CTB 80) are located where the $v_{\text{det,min}}$ is relatively small, i.e., 50 km s^{-1} , whereas W44 is located in a region where $v_{\text{det,min}} \sim 90 \text{ km s}^{-1}$. Table 3 lists $v_{\text{det,min}}$ at the position of each SNR.

In Figure 10, there are many SNRs that are *not* detected in HI 21-cm line in spite of their favorable locations in areas where $v_{\text{det,min}}$ is small. They could be either too young or too old to have an associated fast-expanding HI shell. Their nature can be inferred in Figure 11, which is same as Figure 9, but we now also mark the SNRs without detected HI shells using their minimum velocities for detection. In Figure 11, an SNR without detected HI can be either an old SNR with a velocity less than $v_{\text{det,min}}$ or a young SNR above the grid, i.e., with velocity greater than that at $t/t_{\text{sf}} = 1$. Note that if an SNR is above the grid, it means that the remnant is in adiabatic phase and does not have an HI shell. It is “too young”, i.e., younger than t_{sf} in equation (6). Note that t_{sf} is large when the ambient density is low. For small SNRs, e.g., those with $R_s \leq 10 - 20 \text{ pc}$, the latter possibility is more likely unless they are in a dense environment, such as a molecular cloud. For larger SNRs, both possibilities are likely. Further observational studies will be helpful to address the nature of such SNRs individually.

As a final comment, our study in this paper has targeted *known* SNRs, but there could be many missing SNRs. The estimated SN rate in our Galaxy ranges from 1.4 to $5.8 \times 10^{-2} \text{ yr}^{-1}$ (Li et al. 2011). If we adopt the recent estimate from the Lick Observatory Supernova Search, $2.84 \pm 0.60 \times 10^{-2} \text{ yr}^{-1}$ (Li et al. 2011), the total number of radio SNRs in the Galaxy would be ~ 2800 , assuming $1 \times 10^5 \text{ yrs}$ of visible radio continuum emission. Then, simply using the geometrical fraction of the survey area, which is 18% for a Galactic disk radius of 15 kpc, the expected number of radio SNRs in the survey area is ~ 500 . Therefore, the number of known SNRs (39) is only 8% of the expected population. This small fraction could be due to several factors: faintness of old SNRs in radio continuum, confusion due to Galactic background emission, collective explosions of CCSNe that produce supershells instead of

SNRs, etc. (see Koo & Kang 2004; Higdon & Lingenfelter 2005; Brogan et al. 2006). So in principle, there could be many old SNRs or supershells not visible in radio continuum but visible in the HI 21-cm line, and it may be worthwhile to search for such HI features.

5. Summary

The I-GALFA survey provides fully-sampled HI data covering the Galactic plane between longitudes 32 to 77 degrees and latitudes -10 to $+10$ degrees. The high resolution ($4'$) and high sensitivity (0.2 K) of the data provide an opportunity to investigate small-scale, faint HI emission in the diffuse ISM. In this paper, we have explored the I-GALFA data toward the all known 39 SNRs in order to search for associated fast-expanding HI shells. Our main results are as follows:

1. Among the 39 SNRs in the survey area, four SNRs show associated high-velocity (HV) HI emission. These four SNRs were classified by KH91 as rank 3 SNRs with excess emission at the highest positive velocities in their low-resolution ($30'$) HI study. KH91 listed another SNR (W50) as a candidate with associated HV HI emission out of 26 SNRs known in the survey area at that time. But the high-resolution I-GALFA data show that the emission extends well beyond the SNR boundary, so we consider it not associated with the SNR. Surprisingly, we have not detected associated HV HI emission in any of the ten SNRs discovered since the work of KH91.
2. The four SNRs where we have detected physically associated HV HI gas are G34.7 $-$ 0.4 (W44), G49.2 $-$ 0.7 (W51C), G54.4 $-$ 0.3 (HC40), and G69.0 $+$ 2.7 (CTB 80). Their velocity structures indicate that the HV HI gas is in portions of expanding shells. In the SNR W44, we see HI emission from both receding and approaching portions of the shell, which is the first ever such detection. In the other SNRs, we could see only the receding portions of the shells. The SNR G54.4 $-$ 0.3 shows highly circularly symmetric HI emission that matches very well with its radio continuum morphology. There is a ring structure lying just outside the SNR boundary, which could be a pre-existing structure formed by the progenitor. We discuss the properties of the expanding HI shells in these two SNRs and derive their physical parameters. The other two SNRs have been studied previously in detail. The I-GALFA results are consistent with those previous studies.
3. The four SNRs with associated fast-expanding HI shells are all middle-aged SNRs with $t_s = 1.8 - 9.5 \times 10^4$ yr (Table 2). The expansion velocities of the shells range from 59 to 135 km s $^{-1}$. Notably, their estimated ambient densities are all $\gtrsim 1$ cm $^{-3}$, significantly higher than that of the warm or hot ISM filling most of interstellar space. Two of them have

associated PWN indicating that they are the remnants of CCSNe. The other two do not have PWN but are interacting with molecular clouds, so they are also likely the remnants of CCSNe. Therefore, the SNRs with HI shells (HI SNRs) that are detected are middle-aged SNRs of probable CCSN origin interacting with a relatively dense medium. Large HI SNRs in the diffuse ISM could be detected in principle, but they have not found.

4. The visibility of HI SNRs depends on their location in the Galaxy. Three of the four detected HI SNRs (excluding W44) are located where the visibility is favorable. On the other hand, many SNRs are *not* detected in the HI 21-cm line despite having favorable locations. They could be either too young or too old to have an associated fast-expanding HI shell. We present a diagram (Figure 11) that can be used to infer the nature of these SNRs.

We thank the anonymous referee for the careful review and thoughtful comments on the paper. The Inner Galaxy ALFA (I-GALFA³) survey data are part of the Galactic ALFA (GALFA) HI project⁴ observed with the Arecibo L-band Feed Array (ALFA) on the 305-meter William E. Gordon Telescope. The Arecibo Observatory is a U.S. National Science Foundation facility operated under sequential cooperative agreements with Cornell University and SRI International, the latter in alliance with the Ana G. Méndez-Universidad Metropolitana and the Universities Space Research Association. This work has been supported by the Korean Research Foundation under grant KRF-2008-313-C00372 to B.-C. K.

REFERENCES

- Abdo, A. A., Ackermann, M., Ajello, M., et al. 2010, *Science*, 327, 1103
- Abdo, A. A., Ackermann, M., Ajello, M., et al. 2009, *ApJ*, 706, L1
- Arbutina, B., Urošević, D., Stanković, M., & Tešić, Lj. 2004, *MNRAS*, 350, 346
- Boumis, P., Xilouris, E. M., Alikakos, J., Christopoulou, P. E., Mavromatakis, F., Katsiyannis, A. C., & Goudis, C. D. 2009, *A&A*, 499, 789
- Boumis, P., Mavromatakis, F., Xilouris, E. M., Alikakos, J., Redman, M. P., & Goudis, C. D. 2005, *A&A*, 443, 175

³<http://www.naic.edu/~igalfa>

⁴<https://sites.google.com/site/galfahi/>

- Boumis, P., Meaburn, J., López, J. A., Mavromatakis, F., Redman, M. P., Harman, D. J., & Goudis, C. D. 2004, *A&A*, 424, 583
- Brand, J. & Blitz, L. 1993, *A&A*, 275, 67
- Braun, R., & Strom, R. G. 1986, *A&AS*, 63, 345
- Brogan, C. L., Gelfand, J. D., Gaensler, B. M., Kassim, N. E., & Lazio, T. J. W. 2006, *ApJ*, 639, L25
- Burton, W. B. 1988, in: *Galactic and Extragalactic Radio Astronomy*, 2nd ed., Eds. G. L. Verschuur, K. I. Kellermann (Springer, Berlin) 154
- Case, G. L., & Bhattacharya, D. 1998, *ApJ*, 504, 761
- Castelletti, G., Dubner, G., Brogan, C., & Kassim, N. E. 2007, *A&A*, 471, 537
- Caswell, J. L., Murray, J. D., Roger, R. S., Cole, D. J., & Cooke, D. J. 1975, *A&A*, 45, 239
- Cazzolato, F., & Pineault, S. 2005, *AJ*, 129, 2731
- Chevalier, R. A. 1999, *ApJ*, 511, 798
- Cioffi, D. F., McKee, C. F., & Bertschinger, E. 1988, *ApJ*, 334, 252
- Ehlerová, S., & Palouš, J. 2005, *A&A*, 437, 101
- Fesen, R. A., Saken, J. M., & Shull, J. M. 1988, *Nature*, 334, 229
- Folgheraiter, E. L., Warwick, R. S., Watson, M. G., & Koyama, K. 1997, *MNRAS*, 292, 365
- Frail, D. A., & Clifton, T. R. 1989, *ApJ*, 336, 854
- Froebrich, D., Davis, C. J., Ioannidis, G., et al. 2011, *MNRAS*, 413, 480
- Giacani, E. B., Dubner, G., Cappa, C., & Testori, J. 1998, *A&AS*, 133, 61
- Gibson, S. J., Koo, B., Douglas, K. A., et al. 2012, *American Astronomical Society Meeting Abstracts*, 219, #349.29
- Giovanelli, R., & Haynes, M. P. 1979, *ApJ*, 230, 404
- Giuliani, A., Cardillo, M., Tavani, M., et al. 2011, *ApJ*, 742, L30
- Green, D. A. 2004, *Bulletin of the Astronomical Society of India*, 32, 335

- Green, D. A. 2009a, *Bulletin of the Astronomical Society of India*, 37, 45
- Green, D. A. 2009b, *MNRAS*, 399, 177
- Guseinov, O. H., Ankay, A., Sezer, A., & Tagieva, S. O. 2003, *A&AT*, 22, 273
- Heiles, C. 1979, *ApJ*, 229, 533
- Heiles, C. 1984, *ApJS*, 55, 585
- Heiles, C., & Troland, T. H. 2003, *ApJ*, 586, 1067
- Higdon, J. C., & Lingenfelter, R. E. 2005, *ApJ*, 628, 738
- Jiang, B., Chen, Y., Wang, J., Su, Y., Zhou, X., Safi-Harb, S., & DeLaney, T. 2010, *ApJ*, 712, 1147
- Junkes, N. 1996, *Unsolved Problems of the Milky Way*, 169, 627
- Junkes, N., Fuerst, E., & Reich, W. 1992a, *A&AS*, 96, 1
- Junkes, N., Fuerst, E., & Reich, W. 1992b, *A&A*, 261, 289
- Kim, H.-J., Koo, B.-C., & Moon, D.-S. 2013, in preparation
- Koo, B.-C., Gibson, S. J., Kang, J.-h., et al. 2010, *Highlights of Astronomy*, 15, 788
- Koo, B.-C., & Kang, J.-h. 2004, *MNRAS*, 349, 983
- Koo, B.-C., Kang, J.-h., & McClure-Griffiths, N. M. 2004, *Journal of Korean Astronomical Society*, 37, 61
- Koo, B.-C., & Moon, D.-S. 1997a, *ApJ*, 475, 194
- Koo, B.-C., & Moon, D.-S. 1997b, *ApJ*, 485, 263
- Koo, B.-C., & Heiles, C. 1995, *ApJ*, 442, 679
- Koo, B.-C., Kim, K.-T., Seward, F. D. 1995, *ApJ*, 447, 211
- Koo, B.-C., Yun, M.-S., Ho, P. T. P., & Lee, Y. 1993, *ApJ*, 417, 196
- Koo, B.-C., & Heiles, C. 1991, *ApJ*, 382, 204 (KH91)
- Koo, B.-C., Reach, W. T., Heiles, C., Fesen, R. A., & Shull, J. M. 1990, *ApJ*, 364, 178

- Koralesky, B., Frail, D. A., Goss, W. M., Claussen, M. J., & Green, A. J. 1998, *ApJ*, 116, 1323
- Kothes, R., Uyaniker, B., & Reid, R. I. 2005, *A&A*, 444, 871
- Kothes, R., Landecker, T. L., & Wolleben, M. 2004, *ApJ*, 607, 855
- Kothes, R., Reich, W., Foster, T., & Byun, D.-Y. 2003, *ApJ*, 588, 852
- Kulkarni, S. R., Clifton, T. C., Backer, D. C., Foster, R. S., & Fruchter, A. S. 1988, *Nature*, 331, 50
- Lang, C. C., Wang, Q. D., Lu, F., & Clubb, K. I. 2010, *ApJ*, 709, 1125
- Lee, J.-J., Koo, B.-C., Yun, M. S., Stanimirović, S., Heiles, C., & Heyer, M. 2008, *AJ*, 135, 796
- Levine, E. S., Heiles, C., & Blitz, L. 2008, *ApJ*, 679, 1288
- Li, W., Chornock, R., Leaman, J., Filippenko, A. V., Poznanski, D., Wang, X., Ganeshalingam, M., & Mannucci, F. 2011, *MNRAS*, 412, 1473
- Lockman, F. J., Blundell, K. M., & Goss, W. M. 2007, *MNRAS*, 381, 881
- Lee, H.-G., Moon, D.-S., Koo, B.-C., Lee, J.-J., & Matthews, K. 2009, *ApJ*, 691, 1042
- Lozinskaya, T. A., Sitnik, T. G., & Pravdikova, V. V. 1993, *ARep*, 37, 240
- Marsden, D., Lingenfelter, R. E., Rothschild, R. E., & Higdon, J. C. 2001, *ApJ*, 550, 397
- Markwardt, C. B. 2009, *Astronomical Society of the Pacific Conference Series*, 411, 251 (<http://purl.com/net/mpfit>)
- Matthews, B. C., Wallace, B. J., & Taylor, A. R. 1998, *ApJ*, 493, 312
- Mavromatakis, F., Papamastorakis, J., Ventura, J., Becker, W., Paleologou, E. V., & Schaudel, D. 2001, *A&A*, 370, 265
- McClure-Griffiths, N. M. 2012, *AN*, 333, 497
- McClure-Griffiths, N. M., Dickey, J. M., Gaensler, B. M., & Green, A. J. 2002, *ApJ*, 578, 176
- McClure-Griffiths N. 2001, PhD thesis, Univ. Minnesota

- Peek, J. E. G., Heiles, C., Douglas, K. A., et al. 2011, *ApJS*, 194, 20
- Peek, J. E. G., Begum, A., Douglas, K. A., et al. 2010, *Astronomical Society of the Pacific Conference Series*, 438, 393
- Petre, R., Kuntz, K. D., & Shelton, R. L. 2002, *ApJ*, 579, 404
- Reach, W. T., Rho, J., & Jarrett, T. H. 2005, *ApJ*, 618, 297
- Reich, W., Furest, E., Reich, P., & Reif, K. 1990, *A&AS*, 85, 633
- Rho, J., & Petre, R. 1998, *ApJ*, 503, L167
- Roberts, W. W. 1969, *ApJ*, 158, 123
- Seta, M., Hasegawa, T., Dame, T. M., Sakamoto, S., Oka, T., Handa, T., Hayashi, M., Morino, J.-I., Sorai, K., & Usuda, K. S. 1998, *ApJ*, 505, 286
- Stil, J. M., Taylor, A. R., Dickey, J. M., Kavars, D. W., Martin, P. G., Rothwell, T. A., Boothroyd, A. I., Lockman, F. J., & McClure-Griffiths, N. M. 2006, *AJ*, 132, 1158
- Taylor, J. H., & Cordes, J. M. 1993, *ApJ*, 411, 674
- Taylor, A. R., Gibson, S. J., Peracaula, M., et al. 2003, *AJ*, 125, 3145
- Wolszczan, A., Cordes, J. M., & Dewey, R. J. 1991, *ApJ*, 372, L99
- Wootten, H. A. 1977, *ApJ*, 216, 440
- Yamaguchi, H., Ueno, M., Koyama, K., Bamba, A., & Yamauchi, S. 2004, *PASJ*, 56, 1059
- Yang, J., Zhang, J.-L., Cai, Z.-Y., Lu, D.-R., & Tan, Y.-H. 2006, *Chinese J. Astron. Astrophys.*, 6, 210
- Yoshita, K., Miyata, E., & Tsunemi, H. 2000, *PASJ*, 52, 867

Table 1. Supernova Remnants in the I-GALFA Survey Area and Their Associated High-Velocity HI Gases

G-Name	Other Name	Size (arcmin)	Type	$T_{b,21\text{cm}}$ (K)	KH91 Rank ¹	Note on the High-Velocity HI Gas from This Work
G31.9 + 0.0	3C391	7×5	S	140	1	...
G32.1 – 0.9	...	40?	C?
G32.4 + 0.1	...	6	S	1.7?
G32.8 – 0.1	Kes 78	17	S?	8.6?	2	...
G33.2 – 0.6	...	18	S	2.2	0	...
G33.6 + 0.1	Kes 79	10	S	45	2	...
G34.7 – 0.4	W44	35×27	C	52	3	associated HV HI gas at +124 – +240 and –120 – –67 km s ^{–1}
G35.6 – 0.4	...	15×11	S	9.7
G36.6 – 0.7	...	25?	S?	...	0	...
G36.6 + 2.6	...	17×13?	S	0.6?
G39.2 – 0.3	3C396	8×6	C	74	2	...
G39.7 – 2.0	W50	120×60	?	2.2?	3	HV HI gas at +99 – +124 km s ^{–1} , but extends beyond the SNR
G40.5 – 0.5	...	22	S	4.6	(3)	HV HI gas at –124 – –70 km s ^{–1} , but portion of a larger structure
G41.1 – 0.3	3C397	4.5×2.5	S	401	(3)	HV HI gas at +110 – +120 km s ^{–1} , but probably background emission
G42.8 + 0.6	...	24	S	1.1?	(3)	HV HI gas at +100 – +108 km s ^{–1} , but probably background emission
G43.3 – 0.2	W49B	4×3	S	649	1	...
G43.9 + 1.6	...	60?	S?	0.5?
G45.7 – 0.4	...	22	S	1.8?	0	...
G46.8 – 0.3	(HC30)	17×13	S	13	1	...
G49.2 – 0.7	W51C	30	S?	39?	3	associated HV HI gas at +91 – +160 km s ^{–1}
G53.6 – 2.2	3C400.2	33×28	S	1.6	0	...
G54.1 + 0.3 ²	...	12.4	C	1.9 – 3.8	1	...
G54.4 – 0.3	(HC40)	40	S	3.6	3	associated HV HI gas at +80 – +130 km s ^{–1}
G55.0 + 0.3	...	20×15?	S	0.3?
G55.7 + 3.4	...	23	S	0.5	0	...
G57.2 + 0.8	(4C21.53)	12?	S?	2.5?	0	...
G59.5 + 0.1	...	15	S	2.7?
G59.8 + 1.2	...	20×16?	?	1.0
G63.7 + 1.1	...	8	F	6.1
G65.1 + 0.6	...	90×50	S	0.2
G65.3 + 5.7	...	310×240	S?	0.1?	(3)	HV HI gas at –122 – –159 km s ^{–1} , but no morphological relation
G65.7 + 1.2	DA 495	22	F	2.1	2	...
G67.7 + 1.8	...	15×12	S	1.1
G68.6 – 1.2	...	23	?	0.3?
G69.0 + 2.7	CTB 80	80?	?	3.8?	3	associated HV HI gas at +43 – +110 km s ^{–1}
G69.7 + 1.0	...	16×14	S	1.7
G73.9 + 0.9	...	27	S?	2.7	0	...
G74.0 – 8.5	Cygnus Loop	230×160	S	1.2	0	...
G74.9 + 1.2	CTB 87	8×6	F	38	0	...

Note. — (1) The size is the angular diameter in radio continuum; a single value is quoted for nearly circular remnants, and the product of two values, the major and minor axes, is quoted for elongated remnants. (2) The type codes ‘S’, ‘F’, or ‘C’ represent SNRs with a ‘shell’, ‘filled-centre’, or ‘composite’ radio structure. Uncertain parameters are listed with a question mark. (3) The mean brightness temperature at 21 cm $T_{b,21\text{cm}}$ is calculated from the 1 GHz flux ($F_{1\text{GHz}}$) and spectral index α ($F_\nu \propto \nu^\alpha$) in Green’s catalog, i.e., $T_b = 1.42^\alpha F_{1\text{GHz}} \lambda^2 / (2k\Delta\Omega_S)$ where λ is 21.1 cm and $\Delta\Omega_S$ is the solid angle of the source in steradians. For sources without spectral

indexes, we adopt -0.5 . We use the area of a circle (or ellipse) corresponding to the sizes in Table 1 as the solid angle.

¹Rank ‘3’ SNRs were classified as ‘3’ but regarded to be not-associated with the SNRs by KH91.

²This SNR is classified as type ‘C’ since a larger radio shell at 1.4 GHz is detected by Lang et al. (2010). Its size and surface brightness, which is 100-200 mJy beam⁻¹ with a beam of $6''.82 \times 6''.60$, are used to calculate T_b .

Table 2. Physical Parameters of Supernova Remnants with Fast-Expanding HI Shells

Name	d (kpc)	R_s (pc)	v_0 (km s ⁻¹)	v_{exp} (km s ⁻¹)	Age ($\times 10^4$ yr)	HI Mass (M_\odot)	K.E. ($\times 10^{49}$ erg)	n_0 (cm ⁻³)	E_{SN} ($\times 10^{50}$ erg)	P? ¹	M? ²
W44	2.8	12.5	47	135(2)	2.73(0.04)	393(13)	9.9(0.4)	1.9(0.1)	3.2(0.1)	y	y
W51C ³	6	6	62	96(6)	1.8(0.1)	>1200	>17	~ 100	~ 19	...	y
G54.4 – 0.3	3.3	19.2	40	59(6)	9.5(1.0)	580(150)	2.8(0.9)	0.79(0.20)	1.5(0.5)	...	y
CTB 80 ⁴	2	18.6	13	72(3)	7.7(0.3)	1050(210)	7.6(1.5)	1.5(0.3)	3.8(0.9)	y	...

Note. — The distance (d), radius (R_s), and systemic velocity (v_0) are adopted values, so that they do not have errors. The errors in W44 and G54.4 – 0.3 are formal errors from the fit.

¹Detection (y) of associated pulsars. References are Wolszczan et al. (1991) and Kulkarni et al. (1988) for W44 and CTB 80, respectively.

²Detection (y) of associated molecular clouds. References are Wootten (1977), Koo & Moon (1997b), and Junkes et al. (1992a) for W44, W51C, and G54.4 – 0.3, respectively.

³The HI shell parameters are from Koo & Moon (1997a). W51C is interacting with a molecular cloud, and only a lower limit to the HI mass has been obtained. We adopt 100 cm⁻³ as a characteristic density of the cloud.

⁴The HI shell parameters are from Koo et al. (1990). Koo et al. (1990) obtained an HI mass of 1200 M_\odot by fitting a Gaussian profile to the observed HI mass distribution. But an independent estimate of the mass of the shell is available from infrared studies (900 M_\odot ; see Koo et al. 1990). We adopt the mean of the two as the mass of the expanding shell.

Table 3. Distances to the SNRs in the I-GALFA Survey Area

G-Name	Coordinates		Type	Distance		Radius (pc)	$v_{\text{det, min}}^1$ (km s ⁻¹)	Reference(s)
	ℓ (°)	b (°)		Quoted (kpc)	$\Sigma - D$ (kpc)			
G31.9 + 0.0	31.89	0.03	S	8.5	5.4	7.3	59	Green (2009a)
G32.1 - 0.9	32.12	-0.90	C?	4.6	...	26.8	72	Folgheraiter et al. (1997)
G32.4 + 0.1	32.41	0.11	S	17	33.9	14.8	76	Yamaguchi et al. (2004)
G32.8 - 0.1	32.81	-0.06	S?	~7.1	6.3	17.6	50	Koralesky et al. (1998); Boumis et al. (2009)
G33.2 - 0.6	33.18	-0.55	S	...	10.1	26.4	84	...
G33.6 + 0.1	33.70	0.01	S	7.8 ²	5.1	11.3	53	Frail & Clifton (1989); Green (2004, 2009a)
G34.7 - 0.4	34.67	-0.39	C	2.8 ²	...	12.5	89	Caswell et al. (1975); Green (2004, 2009a)
G35.6 - 0.4	35.59	-0.50	S	3.7	7.6	6.9	76	Green (2009b)
G36.6 - 0.7	36.59	-0.69	S?	53	...
G36.6 + 2.6	36.58	2.60	S	...	20.5	44.3	52	...
G39.2 - 0.3	39.24	-0.32	C	8.5	...	8.6	64	Lee et al. (2009)
G39.7 - 2.0	39.69	-2.39	?	6.0	...	74.0	50	Green (2009a)
G40.5 - 0.5	40.52	-0.51	S	3.8 ³	6.1	12.2	64	Yang et al. (2006)
G41.1 - 0.3	41.11	-0.31	S	10.6 ³	6.1	5.2	94	Jiang et al. (2010)
G42.8 + 0.6	42.82	0.64	S	~6	10.3	20.9	50	Marsden et al. (2001)
G43.3 - 0.2	43.27	-0.19	S	10	4.8	5.0	87	Green (2009a)
G43.9 + 1.6	43.91	1.61	S?	...	5.7	49.7	50	...
G45.7 - 0.4	45.69	-0.39	S	...	9.1	29.1	76	...
G46.8 - 0.3	46.77	-0.30	S	~7.8	5.8	16.9	62	Green (2009a)
G49.2 - 0.7	49.14	-0.60	S?	6	1.9	26.2	51	Koo et al. (1995)
G53.6 - 2.2	53.63	-2.26	S	2.8	6.6	12.4	55	Giacani et al. (1998); Green (2009a)
G54.1 + 0.3	54.09	0.26	C	6	...	10.8	54	Kim et al. (2013)
G54.4 - 0.3	54.47	-0.29	S	3.3 ⁴	3.7	19.2	52	Junkes et al. (1992a); Case & Bhattacharya (1998)
G55.0 + 0.3	55.11	0.42	S	14	23.1	35.3	79	Matthews et al. (1998); Green (2009a)
G55.7 + 3.4	55.60	3.51	S	...	14.3	47.8	76	...
G57.2 + 0.8	57.30	0.83	S?	...	14.3	25.0	74	...
G59.5 + 0.1	59.58	0.12	S	...	11.1	24.2	101	...
G59.8 + 1.2	59.81	1.20	?	...	14.1	36.7	72	...
G63.7 + 1.1	63.79	1.17	F
G65.1 + 0.6	65.27	0.30	S	9	6.8	87.8	93	Green (2009a)
G65.3 + 5.7	65.18	5.66	S?	0.8	2.1	31.7	51	Boumis et al. (2004); Green (2009a)
G65.7 + 1.2	65.72	1.21	F	1.5	...	4.8	51	Kothes et al. (2004); Green (2009a)
G67.7 + 1.8	67.74	1.82	S	~12	18.0	23.4	79	Mavromatakis et al. (2001)
G68.6 - 1.2	68.60	-1.20	?	...	19.2	64.2	50 ⁵	...
G69.0 + 2.7	68.84	2.78	?	2	1.8	23.3	50	Koo et al. (1990)
G69.7 + 1.0	69.69	1.00	S	2 ⁶	13.2	4.4	50	Yoshita et al. (2000)
G73.9 + 0.9	73.91	0.88	S?	~1.3	6.4	5.1	51	Lozinskaya et al. (1993)
G74.0 - 8.5	73.98	-8.56	S	0.44	1.2	12.3	53	Green (2009a)
G74.9 + 1.2	74.94	1.14	F	6.1	...	6.1	75	Kothes et al. (2003); Green (2009a)

Note. — Distance with a symbol of ‘~’ denotes that we adopt the average of possible distances given by reference(s).

¹Minimum expansion velocity for detection.

²Recalculated by Green (2004) assuming a flat rotation curve with $R_{\odot} = 8.5$ kpc and $\Theta_{\odot} = 220$ km s⁻¹.

³Recalculated by this work using the Galactic rotation curve of Brand & Blitz (1993) with $R_{\odot} = 8.5$ kpc and $\Theta_{\odot} =$

220 km s⁻¹.

⁴Recalculated by Case & Bhattacharya (1998) assuming a flat rotation curve with $R_{\odot} = 8.5$ kpc and $\Theta_{\odot} = 220$ km s⁻¹.

⁵This remnant is outside the assumed disk radius of 15 kpc, so we simply adopt 50 km s⁻¹ as the minimum velocity.

⁶Yoshita et al. (2000) suggested that G69.7 + 1.0 will be at a similar distance as CTB 80, since the column density of the ISM between us and G69.7 + 1.0 is analogous with that of CTB 80. In this paper, we adopt 2 kpc for both CTB 80 and G69.7 + 1.0.

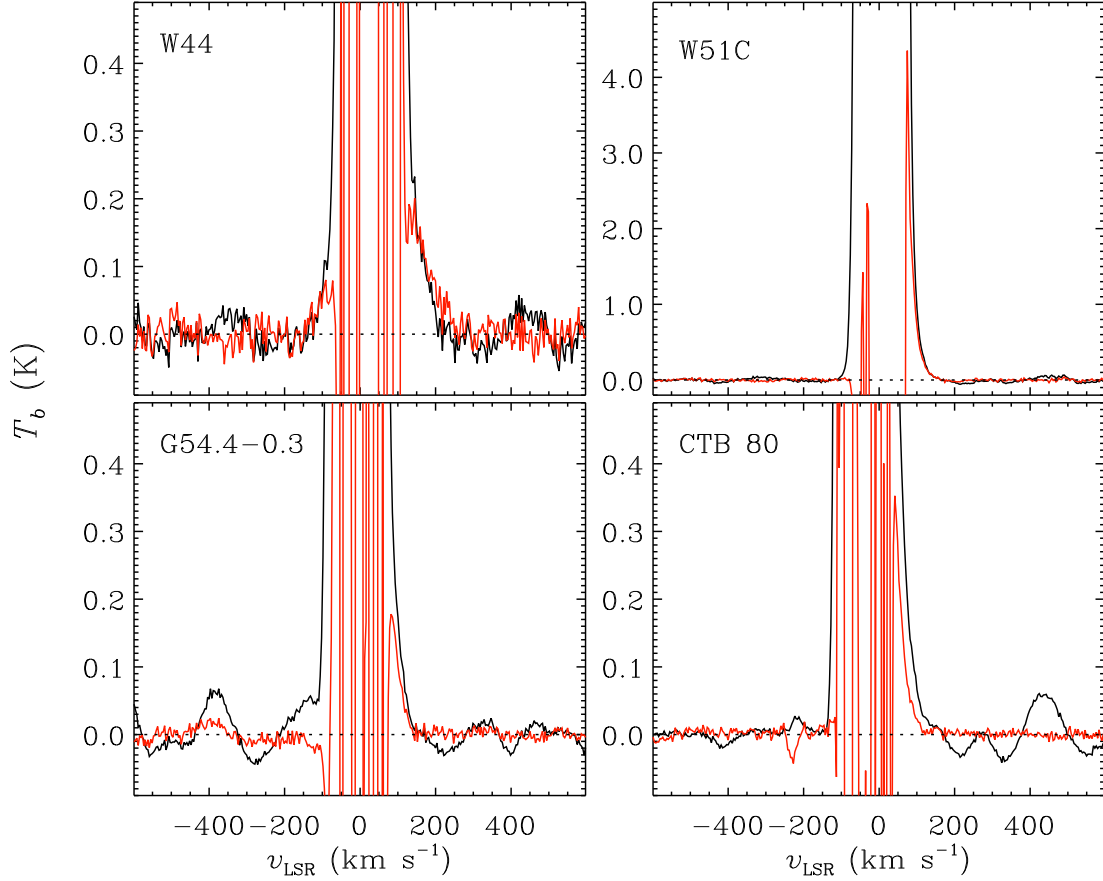


Fig. 1.— Average HI 21-cm line profiles of SNRs that have associated high-velocity HI emission. Average profiles toward the SNRs are in black, while background-subtracted profiles are in red. (See §2 for details of the background subtraction.) Variations in HI 21-cm brightnesses between the source and background directions cause the wild fluctuations in the background-subtracted profiles at low velocities ($|v_{\text{LSR}}| \lesssim 100 \text{ km s}^{-1}$), but these have no effect on our analysis.

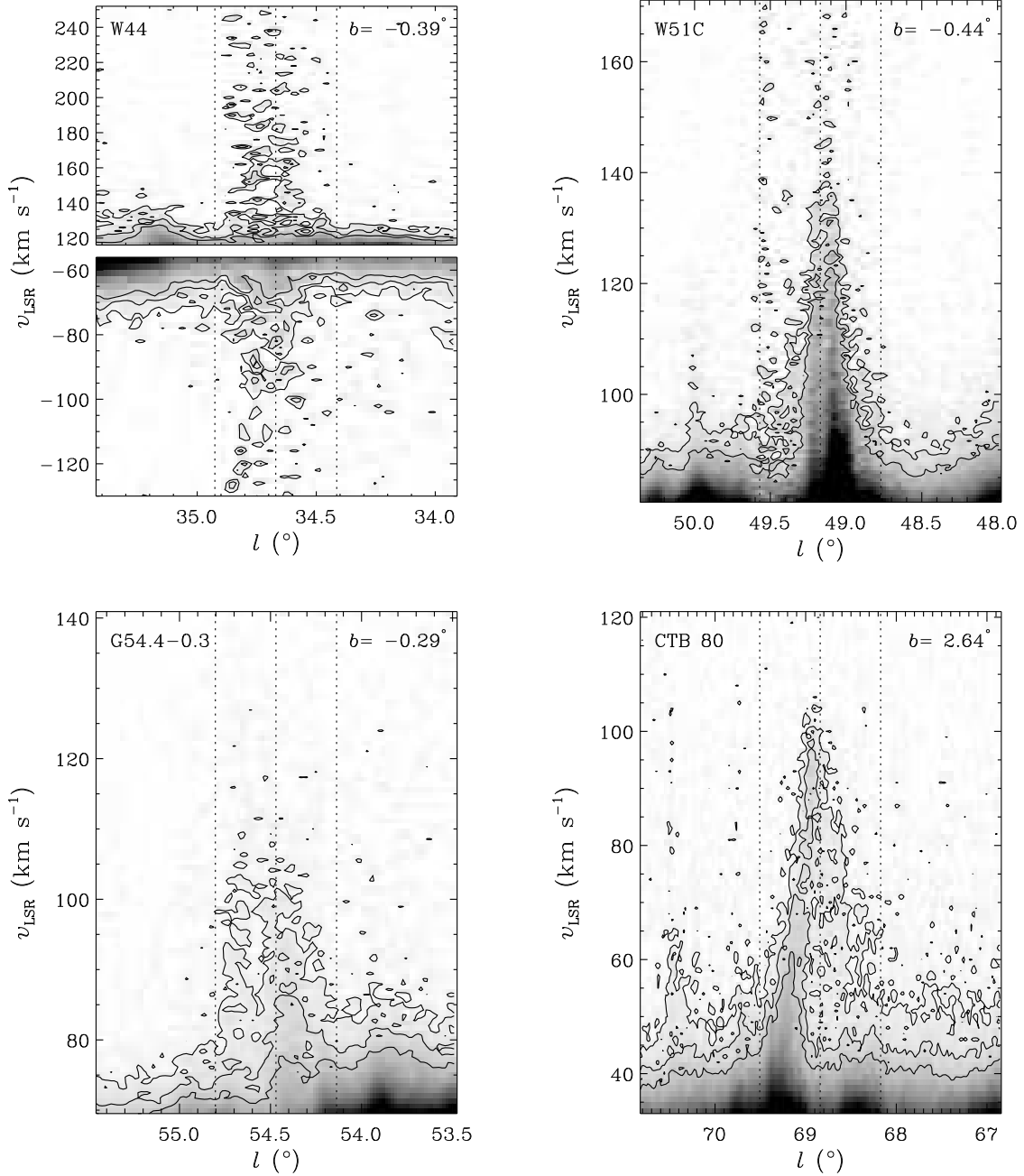


Fig. 2.— I-GALFA (l, v) maps of HI emission of four SNRs. Each longitude-velocity map is at the latitude given in its upper-right corner. The central longitude of the SNR is marked by the middle dotted line in each panel. The other two dotted lines indicate the boundary of the SNR. The gray scale varies from 0 to 5 K (white to black). Contours are 0.5 and 1.0 K for W51C and 0.3, 0.6, and 1.0 K for the other SNRs.

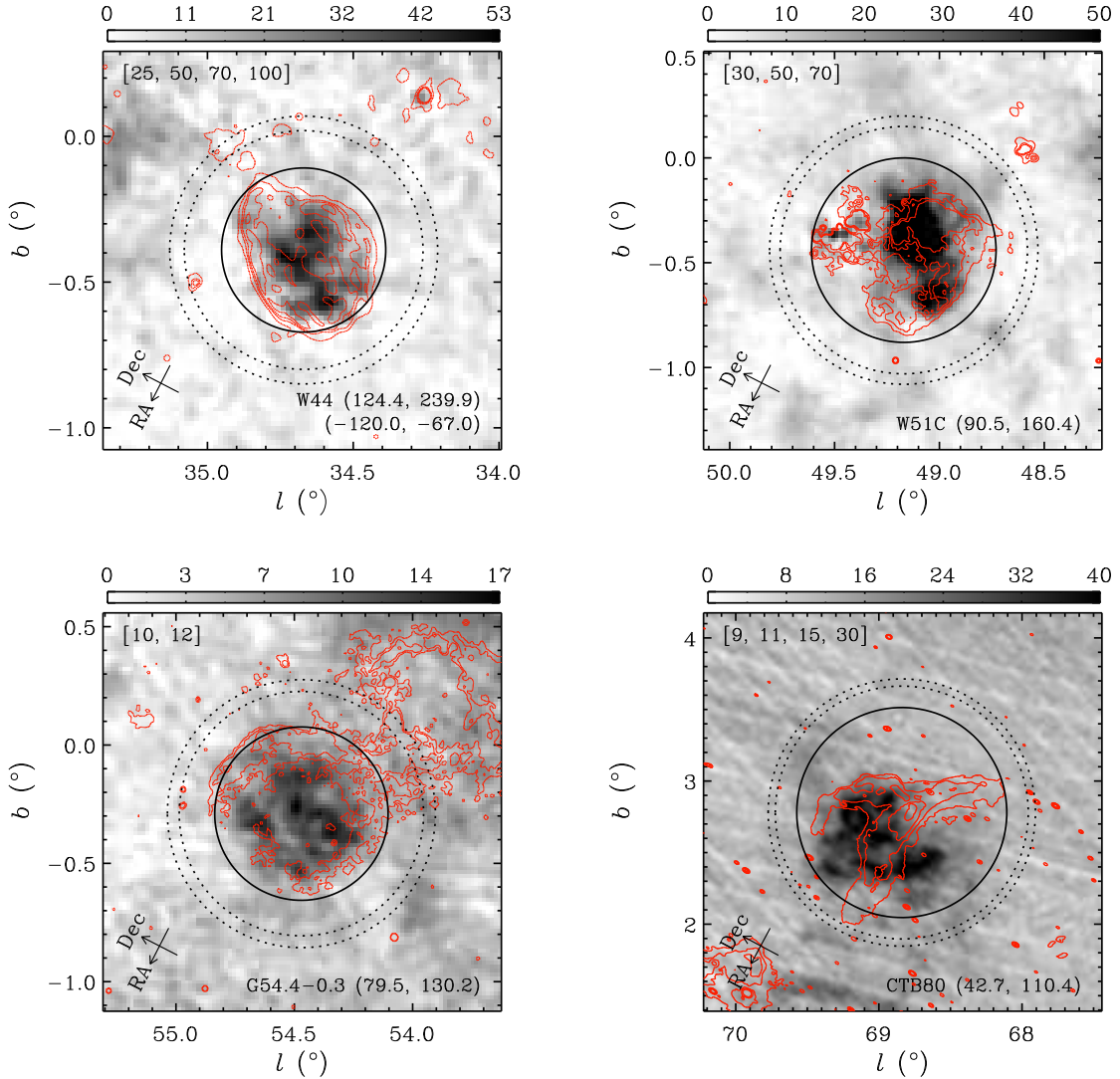


Fig. 3.— HI maps of the fast-expanding HI shells in four SNRs. The lower right corner of each panel gives the SNR name and velocity range for integration in km s^{-1} . For W44, both positive- and negative-velocity HI emissions have been used, although the former dominates. The scale bar units are K km s^{-1} . Red contours show the SNR morphology in 21 cm radio continuum, from the CGPS for CTB 80 and the VGPS for the others. Contour levels are written at the upper left corner of each panel in Kelvins. The black solid circle in each plot shows the mean size of the SNR in radio continuum. Two dotted circles mark the annulus used for estimating the background emission in deriving the average profiles in Figure 1. The size of W51C is $48'$, and other sizes are from Green’s catalog. To aid comparison to literature studies in Equatorial coordinates, arrows are shown in each frame indicating right ascension and declination (J2000) coordinate directions.

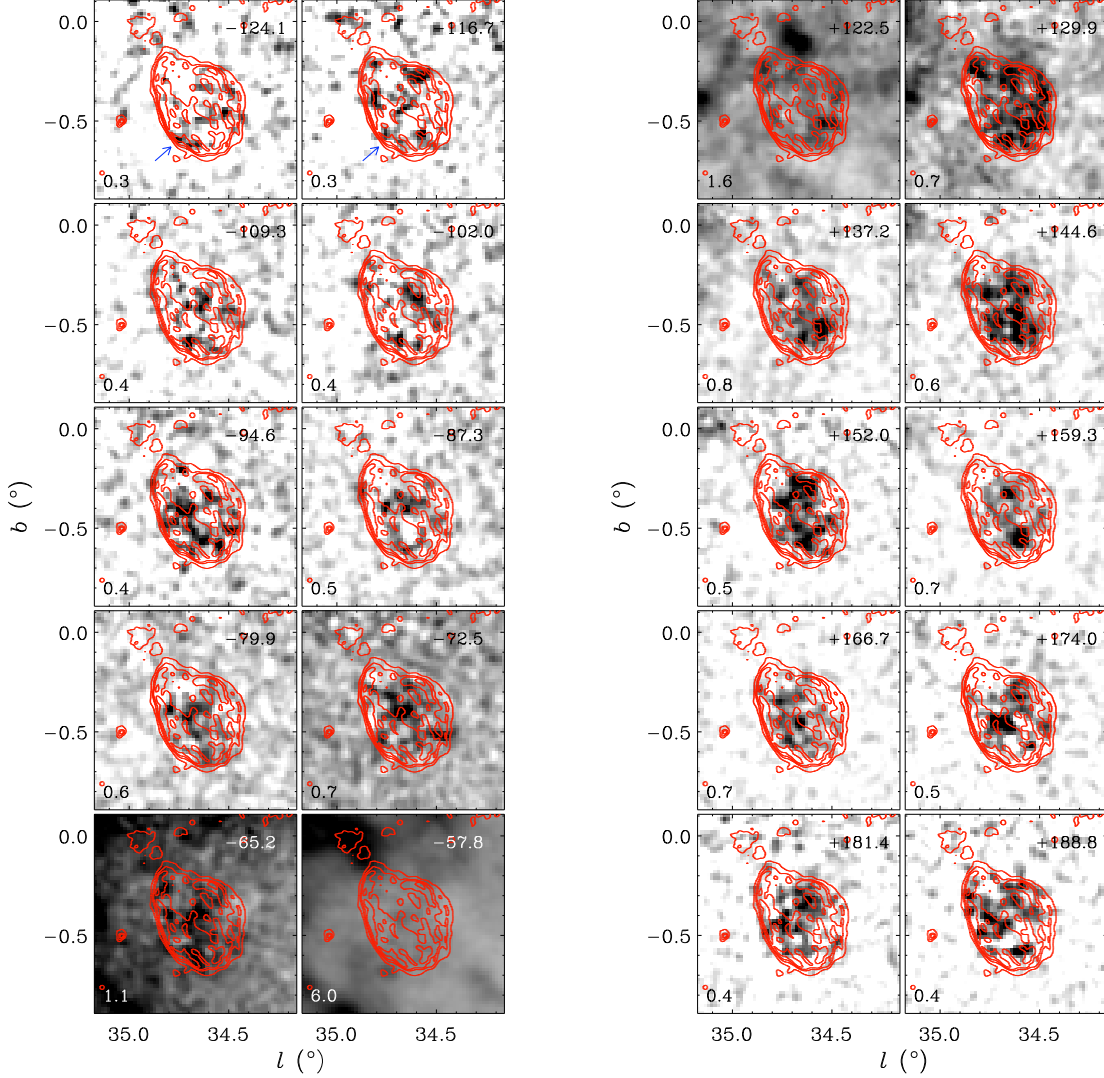


Fig. 4.— Channel maps of HV HI gas associated with the SNR W44 at negative (left) and positive (right) velocities in the I-GALFA HI data. The central LSR velocity of each panel is written at the upper right corner in km s⁻¹. The velocity width of one displayed channel is 3.68 km s⁻¹; this is binned by a factor of 20 from the raw data and has a measured RMS noise of 0.07 K. The HI brightness temperature in each gray scale ranges from 0 K (white) to the value (black) at the lower left corner of each panel in Kelvins. Radio continuum emission at 21 cm is shown by red contours as in Figure 3. The blue arrows in the first two panels indicate an emission feature described in § 3.1.2.

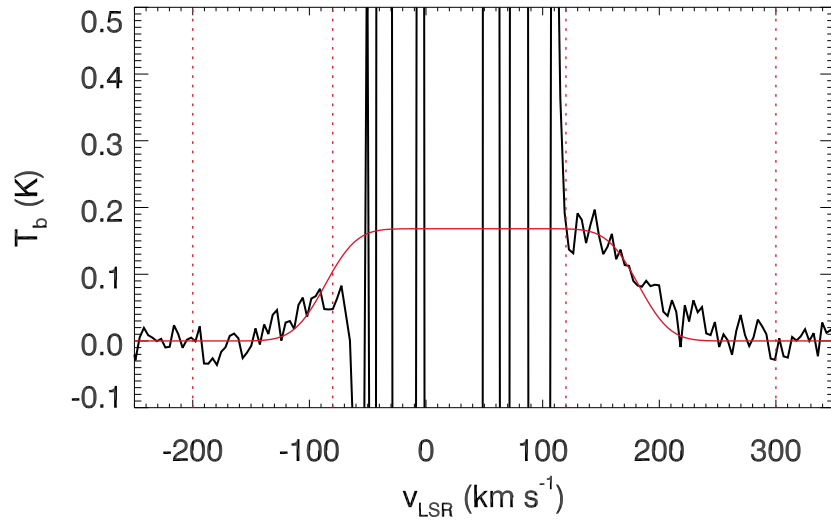


Fig. 5.— A fit to the average background-subtracted HI profile of W44. Low-velocity residual brightness fluctuations are as in Figure 1. The red solid line is a best fit to the profile. The red dotted lines mark the velocity range where the fit has been performed. See §3.1.2 for an explanation of the fit.

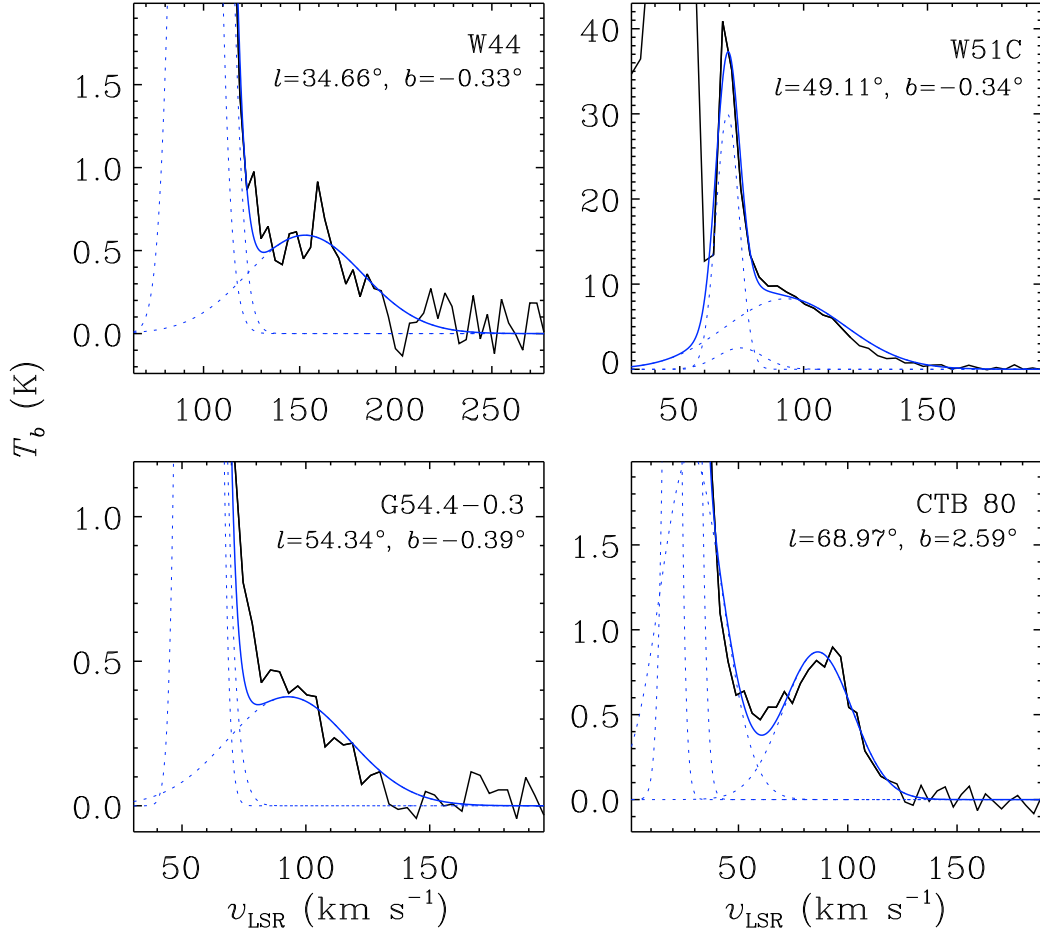


Fig. 6.— HI 21-cm spectra of some prominent HV clumps in individual SNRs (black lines). Their positions are given in the upper right corner of each panel. The HV parts of the spectra have been fitted by several Gaussian components, and the blue dotted and solid lines show the profiles of individual components and their sum, respectively. The components at the highest velocities are the ones related to the fast-expanding HI shells.

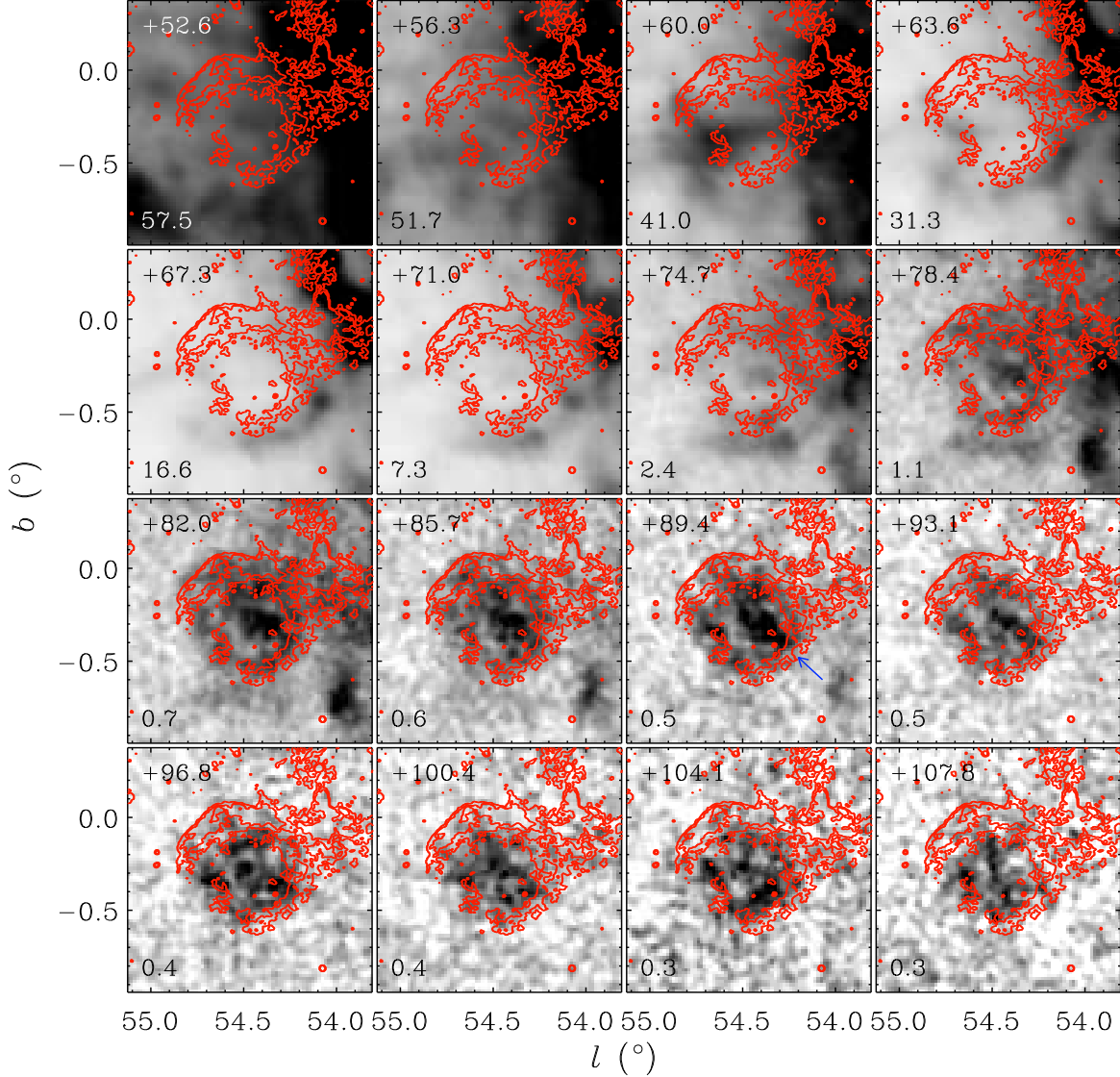


Fig. 7.— Channel maps of HV HI gas associated with the SNR G54.4 – 0.3 in the I-GALFA HI data. As in Figure 4, the central LSR velocity of each panel is shown in the upper left corner in km s^{-1} , and the velocity width of one channel is 3.68 km s^{-1} . The HI brightness temperature in each gray scale ranges from 0 K (white) to the value (black) at the lower left corner of each panel in Kelvins. Radio continuum morphology of the SNR is shown by red contours as in Figure 3. The blue arrow in the $+89.4 \text{ km s}^{-1}$ panel marks an emission feature described in § 3.2.2.

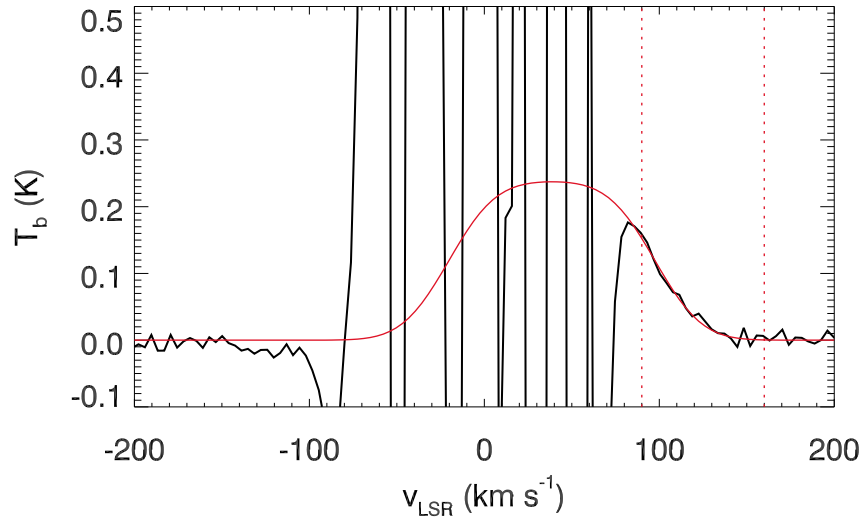


Fig. 8.— A fit to the average HI profile of G54.4 – 0.3. Low-velocity residual brightness fluctuations are as in Figure 1. The red solid line is a best fit to the profile. The red dotted lines mark the velocity range where the fit has been performed. See §3.1.2 for an explanation of the fit.

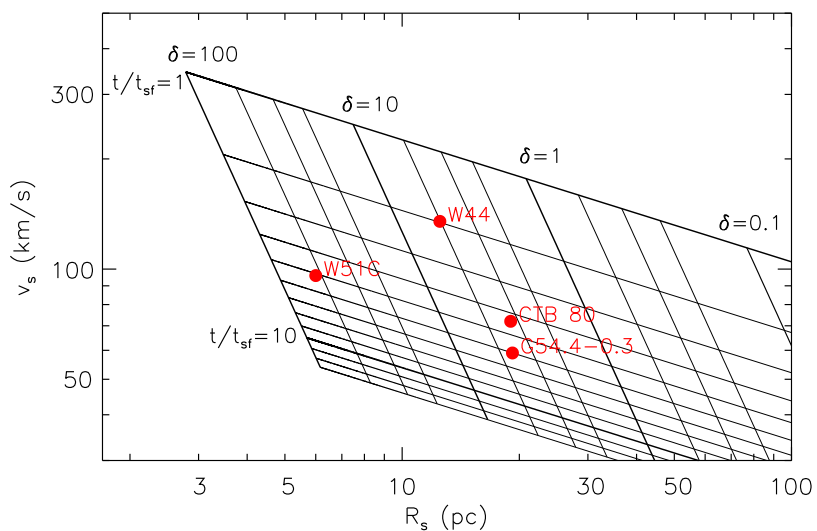


Fig. 9.— Radius-velocity relation of HI SNRs. The grid is for $E_{51} = 1$. The grid shifts along lines of constant δ for different E_{51} but not much: e.g., for $E_{51} = 0.1$, the lines of constant t/t_{sf} shift down by 36%. The thin grid lines in δ are drawn at 20, 30, and 50% of the thick-grid intervals, while those in t/t_{sf} are at every 10%. The four HI SNRs identified in the I-GALFA survey are marked.

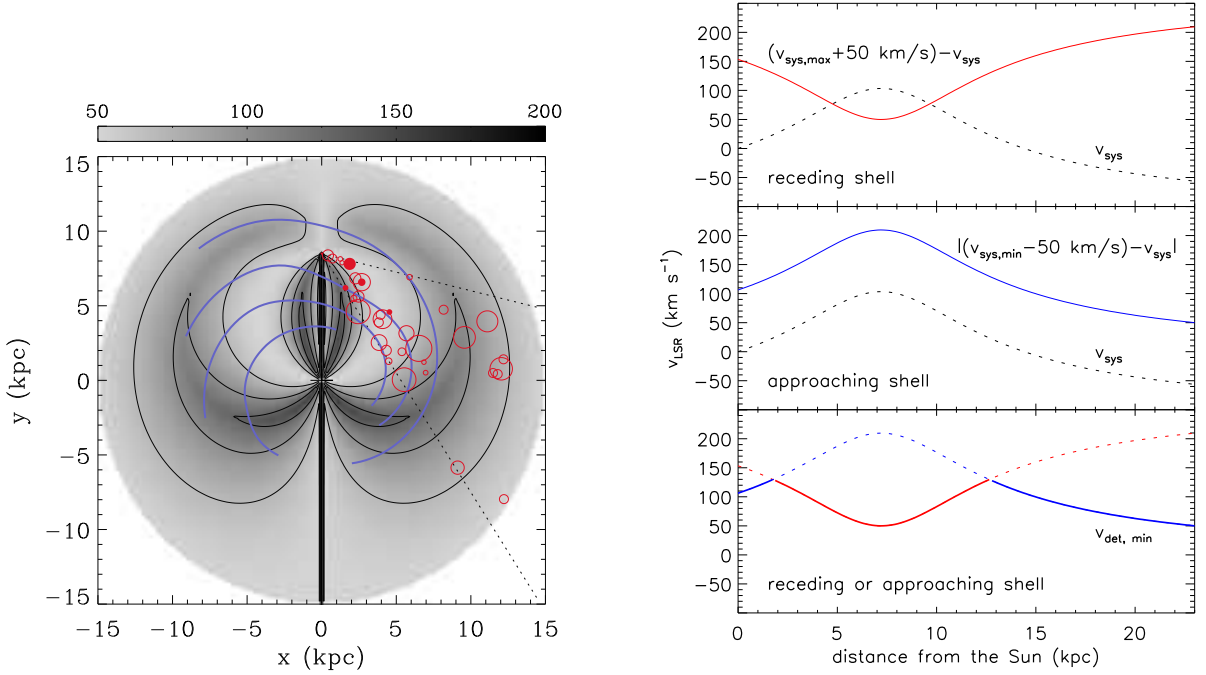


Fig. 10.— (left) Distribution of $v_{\text{det,min}}$, the minimum expansion velocity of a fast-expanding SNR HI shell for detection. Areas with higher minimum expansion velocities are darker. The scale bar at the top displays velocity scales in a unit of km s^{-1} . Contour levels are drawn at 70, 100, and 130 km s^{-1} . The Sun is located at $x = 0.0, y = 8.5$ kpc. The dotted lines mark the boundaries of the I-GALFA survey at $b = 0^\circ$, i.e., $\ell = 32^\circ$ to 77° . The blue curved lines represent the four spiral arms of Taylor & Cordes (1993). The locations of the SNRs in the I-GALFA area are marked by red circles with diameters proportional to SNR size. The SNRs with fast-expanding HI shells are marked by the filled circles. (right) One-dimensional velocity profiles at $\ell = 32^\circ$. Minimum expansion velocities required for the detection of receding (top frame) and approaching (middle frame) portions of the shell are shown together with the systemic LSR velocity (v_{sys}) as a function of distance from the Sun. $v_{\text{det,min}}$ is the smaller of the two velocities (bottom frame). (See text for details.)

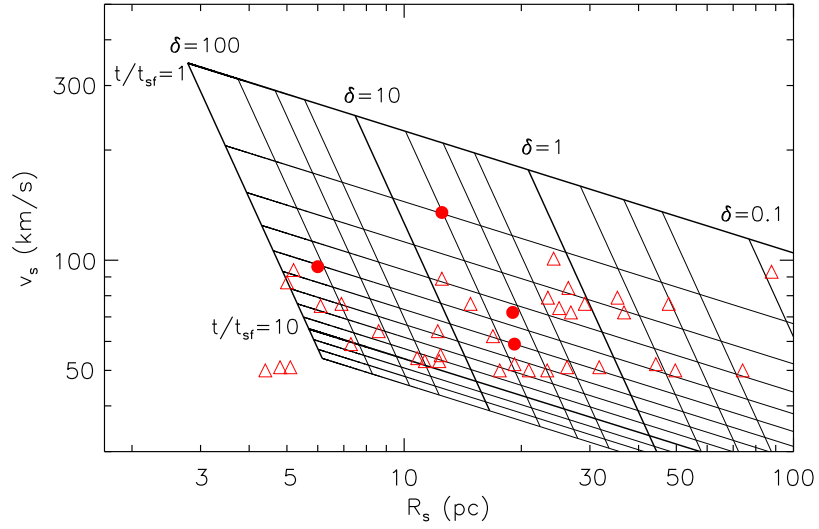


Fig. 11.— Same as Figure 9 but with all SNRs not seen in I-GALFA HI also marked (empty triangles). The velocities of the latter SNRs are the minimum velocities of detection for their hypothetical HI shells. The four SNRs with detected fast-expanding HI shells (filled circles) are shown with their measured expansion velocities.